

Deformation of an Airfoil-shaped Brain Surrogate under Shock Wave Loading

Ling Zhang^a, William J. Jackson^a, Sarah A. Benti^{a,*}

^a*Department of Mechanical Engineering, Iowa State University of Science and Technology, 2529 Union Drive, Ames, IA 50011, USA*

Abstract

Improvised explosive devices (IEDs), during military operations, has increased the incidence of blast-induced traumatic brain injuries (bTBI). The shock wave is created following detonation of the IED. This shock wave propagates through the atmosphere and may cause bTBI. As a result, bTBI research has gained increased attention since this injury's mechanism is not thoroughly understood. To develop better protection and treatment against bTBI, further studies of soft material (e.g. brain and brain surrogate) deformation due to shock wave exposure are essential. However, the dynamic mechanical behavior of soft materials, subjected to high strain rates from shock wave exposure, remains unknown. Thus, an experimental approach was applied to study the interaction between the shock wave and an unconfined brain surrogate fabricated from a biomaterial (i.e. polydimethylsiloxane (PDMS)). The 1:70 ratio of curing agent-to-base determined the stiffness of the PDMS (Sylgard 184, Dow Corning Corporation). A stretched NACA 2414 (upper airfoil surface) geometry was utilized to resemble the shape of a porcine brain. Digital image correlation (DIC) technique was applied to measure the deformation on the brain surrogate's surface following shock wave exposure. A shock tube was utilized to create the shock wave and pressure transducers measured the pressure in the vicinity of the brain surrogate. A transient structural analysis using ANSYS Workbench was performed to predict the elastic modulus of 1:70 airfoil-shaped PDMS, at a strain rate on the order of $6 \times 10^3 \text{ s}^{-1}$. Both compression and protrusion of the PDMS surface

*Corresponding author:

Email address: sbentil@iastate.edu (Sarah A. Benti)

URL: www.me.iastate.edu/sbentil/ (Sarah A. Benti)

were found due to the shock wave exposure. Negative pressure was found in a semi-ring area, which was the cause of protrusion. Oscillation of the brain surrogate, due to the shock wave loading, was found. The frequency of oscillation does not depend on the geometry. This work will add to the limited data describing the dynamic behavior of soft materials due to shock wave loading.

Keywords: bTBI; Polydimethylsiloxane; PDMS; DIC; shock wave; brain surrogate

1. Introduction

Over the years, blast-induced traumatic brain injuries (bTBI) has gained more attention since this topic is not thoroughly understood (Cao et al., 2019; Iwaskiw et al., 2018; Ghajari et al., 2017). This type of injury is classified by four categories: (i) primary injury caused by overpressure, (ii) secondary injury resulting from the impact of flying debris or penetrating objects, (iii) tertiary injury caused by individuals being thrown by the blast wind, and (iv) quaternary injury due to other causes such as heat, smoke, or toxic fumes. The primary injury is caused by the shock wave, which is generated by the improvised explosive devices (IEDs), and can result in eye, ear, lung, and bTBI. Short-term and long-term effects of bTBI, such as inflammation (Cho et al., 2013; Zhang et al., 2014), neuronal loss (Cho et al., 2013), memory loss (Stern et al., 2011), and post-traumatic stress disorder (PTSD) (Kamnaksh et al., 2011) have been studied. However, to develop better personal protection equipment (PPE) against blast-induced injuries to organs (e.g. brain), a deeper understanding of the soft tissue’s deformation is essential.

Blast and shock wave impact experiments have been conducted using animals such as rats (Clemedson and Hultman, 1954; Clemedson, 1956; Readnower et al., 2010; Risling et al., 2011), rabbits (Zhang et al., 2014; Wang et al., 2010), and pigs (Zhu et al., 2013; Säljö et al., 2008). Considering the difficulty of experiments involving laboratory animals, surrogate materials mimicking the brain tissue and skull have been used in blast impact studies. The surrogate skull shapes have included the sphere (Mediavilla Varas et al., 2011; Alley et al., 2011), cylinder (Selvan et al., 2013; Chandra et al., 2012), and ellipsoid (Tan et al., 2016). A Realistic Explosive Dummy (RED) Head, with a skull shape similar to the human skull, has also been fabricated

and used in blast impact studies (Chandra et al., 2017; Ganpule et al., 2013; Hossain, 2010). Materials like poly(methyl methacrylate) (PMMA) (Alley et al., 2011), polycarbonate (Hua et al., 2014), polyurethane (Ganpule et al., 2013; Mediavilla Varas et al., 2011), and aluminum (Chandra et al., 2012) were chosen for the surrogate skulls. Inside the surrogate skulls, the surrogate brain material considered have included fluids such as water (Hua et al., 2014) and oil (Selvan et al., 2013). Soft materials, such as silicone gels (Hossain, 2010; Chanda et al., 2018), gelatin (Alley et al., 2011; Mediavilla Varas et al., 2011), and polydimethylsiloxane (PDMS) silicone elastomer (Alley et al., 2011; Mata et al., 2005; Zhang et al., 2007) have also been considered as a biomaterial and brain tissue surrogate. Alley et al. (2011)’s study showed that Perma-GelTM ballistic gelatin was stiffer and less viscous than the PDMS silicone elastomer. Thus, in this study, PDMS was utilized to create the surrogate brain for investigating deformation under shock wave loading.

Shock wave loading experiments simulating blast wave impact have been conducted using compression-driven shock tubes by researchers to understand the dynamic response of both tissues and tissue surrogates (Bentil et al., 2016; Ganpule et al., 2013; Cernak and Noble-Haeusslein, 2010; Shridharani et al., 2012). A compression-driven shock tube creates reproducible shock waves, which is conducive for a controlled study of blast impact scenarios. Creation of the shock wave, in a compression-driven shock tube, requires separation of the driver and driven section by a diaphragm. The driver section is then pressurized with compressed gas, until the diaphragm ruptures, which generates the propagating shock wave through the driven section. The design details and dimensions of compression-driven shock tubes vary and will influence the shock wave’s peak pressure value and duration. For instance, Ganpule et al. (2013) fixed a realistic explosive dummy (RED) head inside a 711-mm \times 711-mm rectangular cross-sectional compression-driven shock tube with a total length of 12.32 m. In the study by Ganpule et al. (2013), the shock tube consisted of the following sections: driver, transition, straight/extension sections, and catch tank. The peak pressure value’s range and duration of the shock wave was 0.23 MPa – 0.28 MPa and 6 ms, respectively. Hua et al. (2014) also conducted experiments using a 711-mm square shock tube with a surrogate head placed in the test section of the tube. The shock wave peak overpressure and duration was 10.13 MPa and 4.55 ms. The overpressure was different comparing the two studies because the number of diaphragms (0.025-mm-thick Mylar sheets) varied. Selvan et al. (2013)

utilized a compression-driven shock tube with a 229-mm \times 229-mm steel square driven section, a cylindrical driver section, and a transition section. This shock tube could yield an overpressure and duration of 0.2 MPa – 0.3 MPa and 5 ms – 7 ms, respectively.

Digital image correlation (DIC) is a non-contact optical technique for measuring the full-field deformation of surfaces. The DIC method was applied in many areas of science and engineering (Lord et al., 2008; Wang and Cuitiño, 2002; Tung et al., 2010). Biomedical research has also benefited from DIC. For instance, DIC was applied to analyze the movement and deformation of the myocardium during a cardiopulmonary bypass surgery (Hokka et al., 2015; Palanca et al., 2016). DIC was also used to reconstruct the full-field strain response over the surface of the femur at a physiological strain rate (Grassi et al., 2014). Additional biomechanical applications of DIC can be found in a review by Palanca et al. (2016).

There are studies that have focused on applying DIC to characterize the dynamic response of soft materials. For example, *in vivo* deformation measurements of the human heart (Hokka et al., 2015), measurements of the human skin’s mechanical properties (Evans and Holt, 2009; Ottenio et al., 2015), and measurement of Poisson’s ratio of bovine aorta (Zhang et al., 2002) have all utilized DIC. Hong et al. (2016) used the DIC technique to investigate the cavitation damage to a tissue surrogate by a shock wave. In the study, a Hopkinson pressure bar system was applied to simulate the blast pressure wave (Hong et al., 2016). The DIC method can also quantify a soft material’s deformation, due to shock wave exposure, without adhering strain sensors on the surface (Bentil et al., 2016). Adhering sensors on the soft material surface will influence the deformation. Thus, the non-contact DIC approach will be invaluable at describing the interaction of a soft material with a shock wave, in high strain rate experiments. For instance, Sarntinoranont et al. (2011) conducted experiments where a polymer split Hopkinson pressure bar (PSHPB) was coupled with the DIC technique, to visualize the response of the rat brain tissue under high strain rate loading.

The literature reports blast impact experiments and simulations (Alley et al., 2011; Mediavilla Varas et al., 2011; Taylor et al., 2014; Hua et al., 2014; Taylor and Ford, 2009) using a skull or surrogate skull, with and without a brain surrogate, to understand bTBI. However, the presence of the rigid skull presents challenges when investigating the interaction of the brain and shock wave. For instance, Mediavilla Varas et al. (2011) conducted shock tube experiments on a spherical surrogate head, which consisted of a surrogate skull

(polyurethane material) and surrogate brain (gelatin material). The spherical head was located inside a square shock tube. The results showed that the presence of pressure sensors, in the gelatinous brain, hardly disturbed the shock wave’s pressure field (Mediavilla Varas et al., 2011). However, it is unclear how the deformation of the surrogate brain is influenced by the shock wave. This study is one of the first examining the deformation of an unconfined brain surrogate, with a non-symmetrical geometry (i.e. airfoil-shaped), under shock wave loading. Additionally, the dynamic properties of the brain surrogate are also provided from this work.

2. Method and Theory

2.1. Preparation of Airfoil-Shaped PDMS Brain Surrogate

2.1.1. Geometry Choice

The brain surrogate geometry selected is similar to that of a pig’s brain, when viewed from the sagittal plane (i.e. side view of a brain’s hemisphere). The pig brain was chosen since this animal is often used in experiments investigating brain injury (Begonia et al., 2010; Prabhu et al., 2011; Rashid et al., 2012c; Zhang et al., 2011; McCarty et al., 2019; Zhang et al., 2019). This is because pig brains have anatomic similarity of both the vascular system and the gyri and sulci (folds and depressions), when compared with humans (Säljö et al., 2008).

The outline of a pig brain’s hemisphere is geometrically similar to a modified NACA 2414 airfoil. The geometry of NACA 2414 is shown in Figure 1a. To resemble one hemisphere of the pig brain, only the NACA 2414’s upper top half was used (Figure 1b). During experiments by McCarty et al. (2019), to examine the viscoelastic response of shock wave exposed brain tissue, the pig brain’s bottom was fixed on a block to prevent translation by the shock wave. To simulate the shape of the pig brain’s fixed bottom, the horizontal line ($y = 0$) was applied on the modified NACA 2414 airfoil’s geometry (Figure 1c). The modified NACA 2414 airfoil geometry was created by amplifying the x-coordinate by 78 mm and y-coordinate by 300 mm. The amplification ratios were chosen by measuring the size of pig brain samples, which were obtained from a local abattoir. By applying a higher amplification ratio to the y-coordinate, instead of the x-coordinate, the upper airfoil was stretched longitudinally.

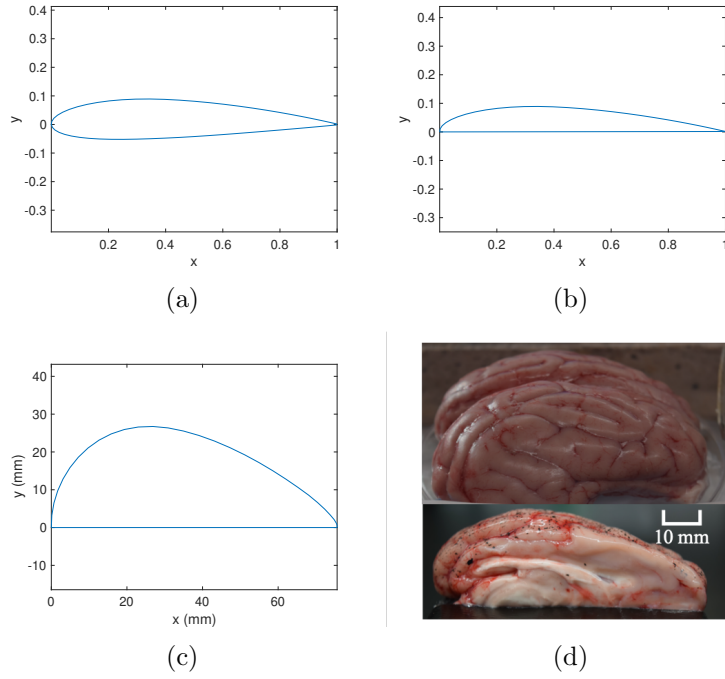


Figure 1: (a) NACA 2414 airfoil geometry, (b) Upper top half of NACA 2414 airfoil geometry, (c) Modified NACA 2414 airfoil geometry using the geometry in (b), and (d) Whole brain (top) and left hemisphere (bottom) of a pig brain from the side view. Occipital lobe and frontal lobe is on the left side and right side of the image, respectively.

2.1.2. Material Choice

Polydimethylsiloxane (PDMS) has been used as a soft tissue surrogate in the biomedical field, due to the consistency, durability, and comparable density with soft biological tissues (Payne et al., 2014). For example, PDMS has been used as the surrogate material to represent skin (Payne et al., 2015; Mahoney et al., 2018), adipose tissues (Payne et al., 2015), and brain (Zhang et al., 2019). As a result, PDMS (i.e. Sylgard 184 PDMS kit) was chosen as the brain surrogate material for this study. The PDMS ratio was determined from a study by Zhang et al. (2019), where the mechanical response of PDMS due to unconfined compression experiments were compared with pig brains. The results showed that under high linear rate compression (e.g. 500 mm/min), PDMS with ratio 1:70 (curing agent:base) by weight or volume (Corning, 2018) has a similar stress response as pig brain tissue. Thus, ratio 1:70 was chosen to fabricate the airfoil-shaped PDMS sample. The PDMS sample was tested at laboratory temperature of 21°C.

2.1.3. Airfoil-Shaped PDMS Brain Surrogate Fabrication

A PA 163 Electronic Balance (Ohaus Corporation) was utilized to weigh the Sylgard 184 base and the total (base and curing agent) solution. The transparent PDMS sample was dyed white to create high contrast images for DIC application (Bentil et al., 2016). Approximately 0.1% titanium dioxide (TiO_2) powder of the total mass was added to the solution to dye the sample. The solution of base, curing agent, and titanium dioxide powder was mixed for 15 minutes. A handmade mold, consisting of four different pieces, was fabricated from aluminum cans (Figure 2a) to facilitate the PDMS curing process. The assembled mold is shown in Figure 2b. The four pieces were connected by cutting notches in aluminum pieces. Aluminum cans were a cost effective option for making the mold. The advantage of assembling pieces, instead of making a one-piece mold, is that the removal of the cured 1:70 ratio PDMS became simpler since it consisted of disassembling the mold.

A cured 1:10 ratio PDMS layer, which was 4-mm thick, served as the base for the mold (Figure 2c). Curing the 1:10 ratio PDMS first ensured that the 1:70 ratio PDMS did not mix with the mold's base. This base prevented the 1:70 PDMS from leaking during the curing process. In addition, parchment paper was attached to the inner surface of the mold shown in Figure 2d. The parchment paper was used to separate the PDMS sample from the mold, after the PDMS was cured, for ease in removal. Once the aluminum mold was assembled, with the cured 1:10 ratio PDMS on the bottom, the uncured 1:70

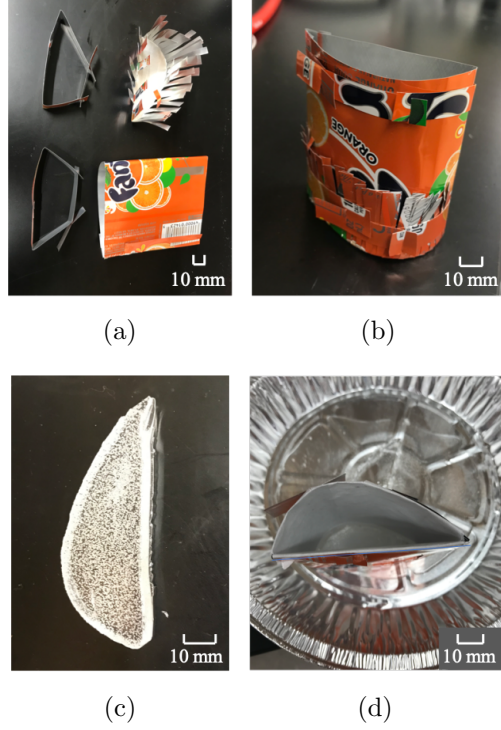


Figure 2: (a) Exploded view of the handmade mold from an aluminum can, (b) The assembled mold for the airfoil-shaped PDMS, (c) Clear 1:10 ratio PDMS that was used as the mold's base, to prevent leaking of the 1:70 ratio PDMS during curing, and (d) The assembled handmade mold with inserted 1:10 ratio PDMS base and parchment paper.

ratio PDMS was poured into the top opening of the mold. The mold, with 1:70 ratio PDMS solution inside, was placed in a vacuum device and degassed for one hour. Then, the sample was placed into a $100^{\circ}\text{C} - 110^{\circ}\text{C}$ heated incubator for two days, to accelerate the curing process. After curing in the heated incubator, the sample rested inside the mold at room temperature for two days. Finally, the 1:70 ratio PDMS sample was separated from the parchment paper and the 1:10 ratio PDMS base. Figure 3 shows the cured and speckled 1:70 ratio airfoil-shaped PDMS brain surrogate. The speckles are small spots generated on the PDMS surface using black spray paint.

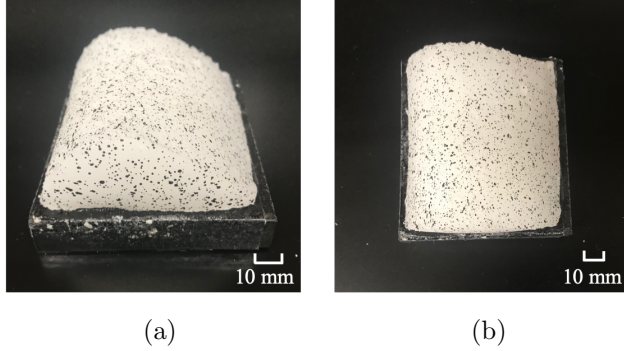


Figure 3: Airfoil-shaped PDMS brain surrogate: (a) Front view, and (b) Top view. The black dots on the samples surface are speckles, which are tracked during the DIC analysis to obtain deformation.

2.2. Experimental Setup for Shock wave Exposure

2.2.1. Shock Tube Setup

Figure 4 shows the setup for the shock wave exposure experiment, which included high-speed digital cameras (Photron, FASTCAM SA-Z) to facilitate DIC analysis. A custom-built compression-driven shock tube, fabricated from a 3/4-in. (19.05-mm) Schedule 80 polyvinyl chloride (PVC) pipe, generated the shock wave. The shock tube was rigidly fixed to an optical table. The length of the shock tube's driver and driven section is 12 cm and 55 cm, respectively. Dead soft aluminum diaphragm, cut into a square shape with a thickness of 0.0025 cm and length of 3 cm, separated the driver and driven section. The driven section was open at the end. An air compressor (Central Pneumatic, 5-gal) was used to pressurize the driver section until the diaphragm ruptured, which created the shock wave that propagated through the driven section. A picture of the diaphragm, from one of the experiments, is shown in Figure 5.

2.2.2. Pressure Transducers Setup

Three high frequency integrated circuit piezoelectric (ICP) pressure transducers (PCB Piezotronics, Model 102B15) were utilized to study how the propagating shock wave changes both inside and outside of the shock tube. The locations of the three pressure transducers are shown in Figure 6, where pressure transducer 1 was closer to the driver section, pressure transducer 2 was closer to the shock tube exit, and pressure transducer 3 was 20-mm away from the shock tube exit. Pressure transducer 1 and 2 were screwed in tapped

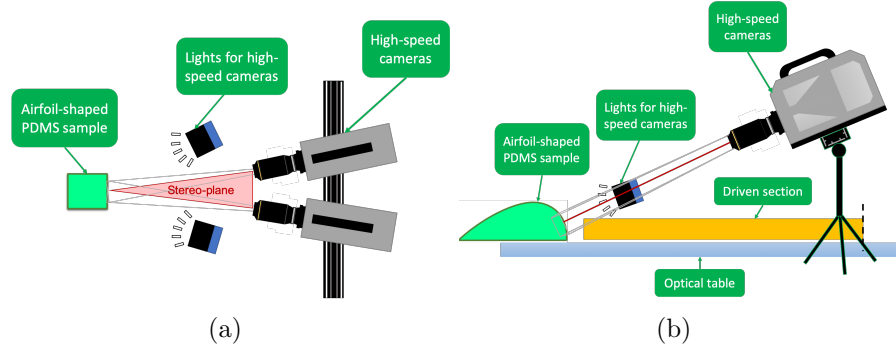


Figure 4: The experimental setup for the airfoil-shaped 1:70 ratio PDMS sample exposed to a shock wave. (a) Top view and (b) Side view.

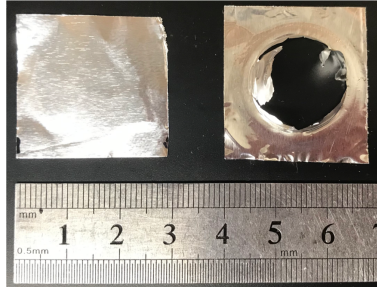


Figure 5: Dead soft aluminum diaphragms separating the driver and driven section of the compression-driven shock tube: (left) unruptured diaphragm and (right) ruptured diaphragm.

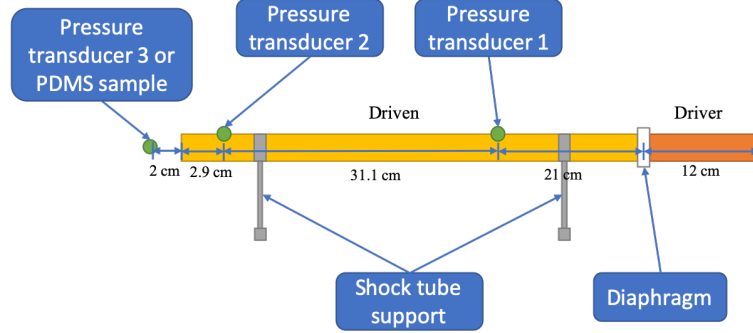


Figure 6: Experimental setup and dimensions of the compression-driven shock tube, along with the locations of the three pressure transducers (not to scale).

holes in the driven section. The bottom surface of pressure transducer 1 and 2 were aligned with the driven section’s inner surface, to minimize disruption of the shock wave pressure profile due to the protruding sensors.

2.2.3. DIC Setup

Two synchronized high-speed digital cameras (Photron, FASTCAM SA-Z) imaged the deforming specimen at a frame rate of 100,000 fps, with a resolution of 640×280 . Experiments at 100,000 fps requires substantial lighting levels. LED lights (Nila, Zaila Deluxe Daylight) were used as the light source. A 105-mm macro lens (Nikon, AF-S VR Micro-NIKKOR 105mm f/2.8G IF-ED) was used for both cameras. The temporal and imaging area’s spatial resolution was $10 \mu\text{s}$ and 0.076 mm/pixel , respectively.

Only one PDMS sample was fabricated for this study, which was speckled using a black spray paint with a flat (i.e. matte) finish. Since the same speckled sample was used multiple times, the speckling pattern was consistent across all the shock wave experiments. The PDMS sample was then adhered to the surface of a rigid block with super glue. The block was immobilized during the shock tube experiment. The front edge of the PDMS airfoil, on the block, was placed 20-mm away from the shock tube exit. Due to limitation of the cameras’ positioning, if the sample is too close to the shock tube exit, the PDMS surface’s center area would be blocked from the cameras’ field-of-view by the driven section’s end. Thus, 20-mm distance was chosen because the whole sample surface can be captured by the camera.

The airfoil’s front and back surface were exposed to the shock wave, in a frontal impact experiment where the aforementioned surfaces faced the shock

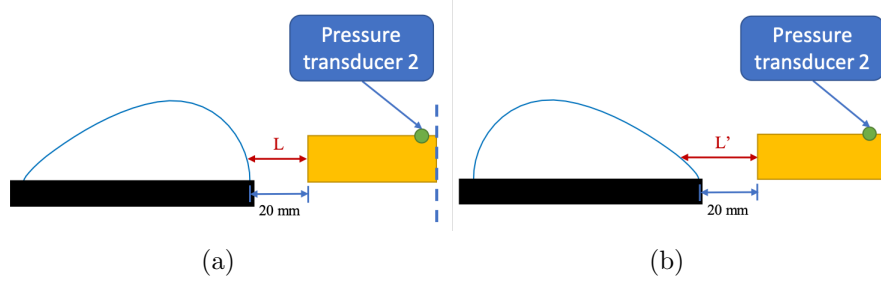


Figure 7: Schematic diagram illustrating the difference between frontal surface and back surface impact, when the airfoil-shaped PDMS is placed 20-mm away from the shock tube exit. (a) Frontal surface and (b) Back surface. L and L' is the distance traveled by the shock wave, before reaching the airfoil-shaped PDMS sample, after exiting the shock tube.

tube exit. Figure 7 illustrates placement of the airfoil-shaped PDMS at the 20-mm distance. The horizontal distance L , which is between the center of the shock tube end and the front surface of the sample, is 21.8 mm. The distance L' is 29.8 mm. During the shock wave experiment with the airfoil-shaped 1:70 ratio PDMS, only pressure transducer 3 was not used. The rigid pressure transducer 3 was not attached to the soft PDMS sample, to prevent the transducer's presence from influencing the sample's deformation.

Three-dimensional digital image correlation analysis (3D-DIC) was used to capture the full-field deformation of the speckled airfoil-shaped PDMS sample, due to shock wave exposure. Calibration of the cameras were conducted, before each experiment, using the principle of stereo-triangulation (Bentil et al., 2016). During the calibration, the block with adhered sample was first removed. Then, a standard rigid calibration target having a size of 14 dots \times 10 dots, with dot spacing of 3 mm was placed in front of the stereo camera pair. The calibration target was then moved around in three-dimensional space and an average of 20 images were acquired during the motion. Images of the calibration target were then analyzed using the commercial software VIC-3D to check the calibration score (VIC3D, 2017). A calibration score of 0.047 was obtained each time, which was below the maximum value of 0.05 specified by VIC3D (2017) to minimize measurement errors associated with 3D-DIC analysis. Following analysis of the calibration target images, measurement bias from 3D-DIC was removed and a three-dimensional coordinate system on the specimen's surface was defined. Shock wave experiments commenced after the calibration.

Following the shock wave experiments, images from two high-speed digi-

tal cameras that were positioned in stereo were exported for 3D-DIC analysis using VIC-3D (VIC3D, 2017). During the 3D-DIC analysis, the PDMS displacement (in-plane and out-of-plane) was tracked by matching subsets of speckles. Lagrangian strain was then computed from the measured displacement. VIC-3D’s default subset size and step size of 29 pixels and 7 was applied, respectively.

2.3. Finite Element Modeling

Finite element (FE) modeling was performed to describe the dynamic response of the airfoil-shaped PDMS sample under shock wave loading. Specifically, a transient structural analysis using ANSYS Workbench (Ansys 17.0, 2019) was conducted. The geometry was generated by using the modified airfoil coordinates in Figure 1c. Figure 8a shows that the edges of the airfoil-shaped PDMS sample, in the FE model, were rounded with a radius of 1 mm to minimize the discretization error during meshing. A hex-dominant mesh, shown in Figure 8a, was used because it has better performance when modeling incompressible soft materials (Gurev et al., 2015). Following a mesh convergence study, the selected mesh contained 34,000 elements.

The boundary condition for this simulation is shown in Figure 8b. The bottom surface of the sample (surface A) was fixed. Three zones (B, C, and D) were generated on the front surface for pressure distribution application. An ANSYS Fluent simulation was used to predict three different pressures, for each of the three zones, by using the pressure at 20-mm away from the shock tube exit as the loading condition. Wall boundary conditions were applied to the shock tube. The driver and driven sections of the shock tube were separated, with a pressure of 3.2×10^5 Pa applied in the driver section at the beginning of the simulation. The Wilcox $k - \omega$ turbulence model (Wilcox, 1988) was utilized.

The airfoil-shaped PDMS, with ratio 1:70, was modeled as linear elastic (elastic modulus = 19 kPa and Poisson’s ratio = 0.499). The elastic modulus’ magnitude was obtained iteratively, such that the peak out-of-plane displacement (W) would compare with the 3D-DIC measurements. Rayleigh damping, which considers damping as a linear combination of the mass and stiffness matrices shown in Equation 1, was used to provide an energy-dissipation mechanism for the 1:70 PDMS. The corresponding Rayleigh damping coefficients for the aforementioned elastic modulus are: $\alpha = 91.5 \text{ s}^{-1}$ and $\beta = 0.005 \text{ s}$. The density of PDMS was 965 kg/m^3 . In the simulation, the

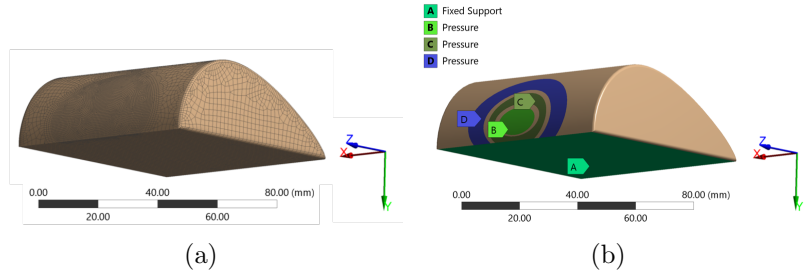


Figure 8: Geometry, mesh, and the boundary condition: (a) the geometry and mesh of airfoil-shaped PDMS sample and (b) boundary condition of simulation.

damping coefficients α and β were adjusted to generate the out-of-plane displacement delay for PDMS exposed to a shock wave. Increasing β -damping will increase the displacement delay.

$$[C] = \alpha[M] + \beta[K], \quad (1)$$

where $[C]$ is the Rayleigh damping, $[M]$ is the mass matrix, and $[K]$ is the stiffness matrix.

Large deflection was activated for the simulation. The total time of the simulation was divided into seven stages. Variable time steps, ranging from $10^{-4}s$ to $10^{-6}s$, were utilized for each stage. In this way, the time needed to run the simulation can be reduced when compared with using a uniform time step throughout each stage. Additionally, the smallest time step of $10^{-6}s$ was applied when the pressure increased dramatically, to prevent solution divergence and mesh crush.

3. Results

3.1. Pressure-time History

Pressure-time traces at the three different pressure transducer (P1, P2, and P3) locations, following eight experiments using the shock tube, are shown in Figure 9. The pressure-time trace results show that the shock wave pressures are consistently generated. Additionally, the results in Figure 9 show how the propagating shock wave pressure changes with time and location. Comparing pressure at P1 and P2, which were captured by the two pressure transducers on the driven section, the duration of the incident pressure curve decreases when the shock wave approaches the shock tube exit

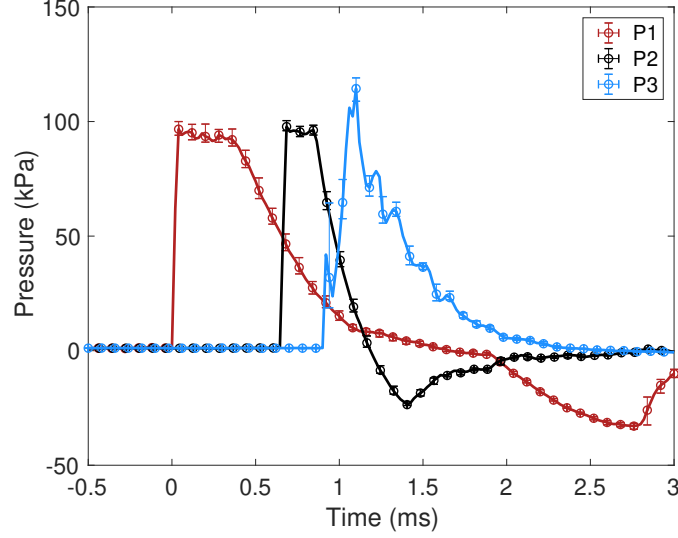


Figure 9: Pressure-time trace from pressure transducer 1 (P1), pressure transducer 2 (P2), and pressure transducer 3 (P3) at 20-mm distance. Eight trials of the pressure-time trace were averaged and are shown for the three pressure transducer locations, along with the error bars denoting the standard deviation. All pressures are gauge.

(i.e. end of the driven section). However, the peak pressure remains the same (about 100 kPa). The pressure curve at P3 (at the end of shock tube) has two peaks. The pressure for the first peak is the incident pressure and is 40 kPa, which is lower than the P1 and P2 since this pressure is outside of the shock tube. The second peak in P3 is the reflected pressure wave, which has a maximum pressure of 115 kPa. The reflected pressure is higher than the incident pressure captured at P1 and P2, as expected. Using the pressure transducer data from Figure 9, the calculated shock wave speed was 455 m/s (Mach 1.3).

3.2. Displacement, Principal Strain, and Shear Strain

3.2.1. Analysis of Out-of-Plane Displacement Plots

By using digital image correlation (DIC) techniques, the out-of-plane displacement was analyzed. Five locations (center, bottom, top, left side, and right side) in Figures 10 were selected to show the deformation measurements. The locations on the front surface were labeled as F1 – F5, while the locations on the back surface were labeled as B1 – B5. The distance between

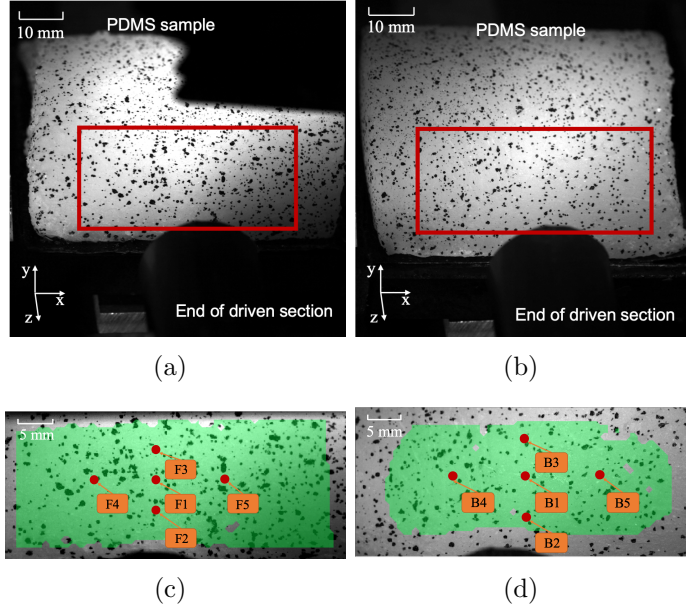


Figure 10: Full-view (1024×1024 resolution) of airfoil-shaped PDMS at 20-mm away from the shock tube exit: (a) the **frontal** surface; (b) the **back** surface. The shaded area, on the right corner of (a), is due to the camera's view being blocked by the light source. The selected locations (red dots) on the airfoil-shaped PDMS' area-of-interest (green), from the 3D-DIC analysis at: (c) the **frontal** surface and (d) the **back** surface. The end of the driven section is the black region. The red rectangle in (a) is the entire region (640×280 resolution) shown in (c), while the red rectangle in (b) is the entire region (640×280 resolution) shown in (d). Even though parts of the sample's surface was blocked by the light source in (a), the area-of-interest inside the rectangle was not blocked. The area-of-interest in (c) and (d) are for the undeformed sample, at time = 0 ms.

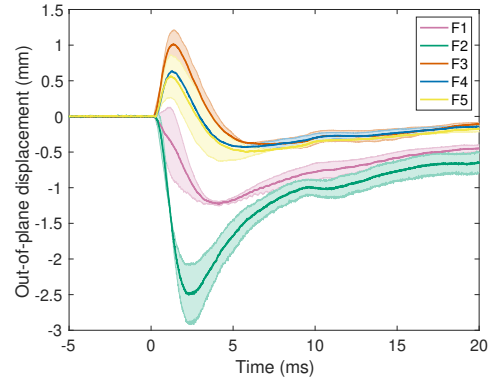
the center point (e.g. F1 or B1) and its respective surrounding points are not all the same, to better capture the range of time histories for the out-of-plane displacements. Selecting points with equal distance, relative to F1 or B1, would have yielded duplicate out-of-plane displacements within the area-of-interest. The out-of-plane displacement (W) results are shown in Figure 11. The sample surface was exposed to a shock wave multiple times, with a 30 minute time gap between each shock wave experiment. This duration accounted for the time needed to save the images from each of the two cameras and recalibrate the system using the calibration target since the focus was adjusted. Table 1 summarizes the number of times each surface was exposed to the shock wave.

Table 1: Number of experiments at each surface of the airfoil-shaped PDMS.

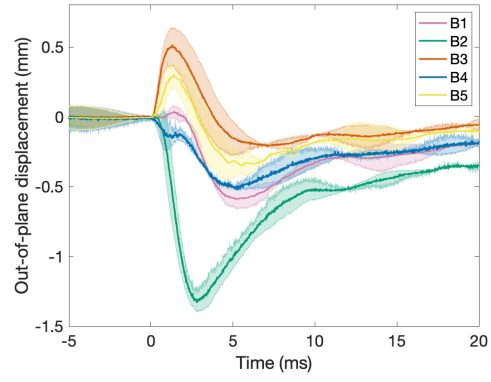
Surface	Number of Experiments
Frontal	2
Back	2

Both positive and negative out-of-plane displacements were captured by cameras. The positive out-of-plane displacement showed protrusion towards the cameras, while the negative displacement showed compression away from the cameras (Figure 4). Figure 11 displays the averaged out-of-plane displacement for all locations. The shaded area show the standard deviation. The out-of-plane displacement results were consistent across all experiments, which implies that the airfoil-shaped brain surrogate’s material property was not changing after exposure to multiple shock waves. When shock wave exposure occurred on the front surface, the maximum negative averaged out-of-plane displacement was 2.49 mm, which is at location F2 (bottom). The maximum positive peak averaged out-of-plane displacement was 1.01 mm at F3. At location F1 and F2, the out-of-plane displacement showed compression behavior. Locations F3, F4, and F5 showed similar positive displacement, with lower absolute peak value than negative peak. The region between location F1 and F3 is a transition area between compression and protrusion. The compression and protrusion started at the same time. However, the positive (protrusion) out-of-plane displacement reached the maximum value and began to decrease before the peak negative (compression) out-of-plane displacement was reached. The duration of the negative out-of-plane displacement was 15 ms.

The averaged out-of-plane displacement for the back surface of the airfoil-shaped PDMS was also shown in Figure 11. Similar to the front surface, both positive and negative out-of-plane displacements exist, although the magnitudes were lower. The lower out-of-plane displacement magnitudes was attributed to the back surface having a different angle of inclination, when compared with the front surface (Figure 1c). Thus, the back surface inclination increased the distance travelled by the shock wave, from L to L' , before contacting the airfoil-shaped PDMS sample (Figure 7). Consid-



(a)



(b)

Figure 11: Averaged out-of-plane displacement for the airfoil-shaped PDMS placed at 20-mm away from the shock tube exit: (a) **frontal** surface and (b) **back** surface. The shaded area show the standard deviation.

ering locations B3 and B5 for the back surface of the airfoil-shaped PDMS sample, following a small positive peak, a negative out-of-plane displacement was measured. At locations B1, B2, and B4, only negative peak out-of-plane displacement exists. The maximum absolute value for the negative averaged out-of-plane displacement was 0.50 mm, while the maximum negative averaged out-of-plane displacement was 1.32 mm.

Comparing the front surface and back surface impact experiments, the absolute value of maximum positive and negative out-of-plane displacement on the front surface was higher than the back surface. The displacement result at F4 was different from B4, while the other results show similar trends at corresponding locations (e.g. F1 and B1). Although the out-of-plane displacements were different between front and back surface, the averaged ratio of maximum and minimum displacement was 0.41 for front surface and 0.38 for back surface. The percent difference, comparing the frontal surface and back surface, was 67.5% for the magnitude of positive averaged out-of-plane displacement and 61.4% for the magnitude of negative averaged out-of-plane displacement. The percent difference for the absolute peak value (between the negative and positive out-of-plane displacement) was 84.6% and 90.1% for the frontal surface and back surface, respectively. The duration of the negative out-of-plane displacement was 120% different than the positive W duration.

3.2.2. Analysis of Contour Plots

The contour plots for the out-of-plane displacement (W), maximum principal Lagrangian strain ($e1$), and the shear Lagrangian strain (exy) at particular times following shock wave exposure, for the PDMS sample's frontal surface, are shown in Figure 12. A negative W displacement was generated in the center area, when the shock wave applied pressure on the PDMS' surface. At the same time, a semicircular ring containing positive W values was generated. This positive W region was the protrusion of the PDMS sample, in the region outside of the center area being compressed. The protrusion was towards the cameras. As time progressed, compression of the center area increased and the protruding region moved upwards (i.e. away from the shock tube) and decreased in out-of-plane displacement magnitude. Both of these areas (positive and negative) were moving upwards as time progressed and was attenuating. After time of 1.51 ms, while the negative area was increasing due to continued compression, the positive area was disappearing. After that behavior, the negative area reduced in size before the sample

returned to a state of zero out-of-plane displacement.

From the maximum principal Lagrangian strain contours, the highest strains are located in a semicircular area and reached a maximum value at 1.85 ms. At the same time, the negative out-of-plane displacement reached its minimum value. Furthermore, the results showed that the maximum principal strain attenuated faster than the out-of-plane displacement. The shear Lagrangian strain contour plots showed two high shear strain zones (a positive and a negative shear strain area), which were symmetric. The symmetry of these two areas showed that the left and right area were under similar shear deformation conditions, but in the opposite direction. After the highest shear strain was reached, it attenuated with the maximum principal strain. The percent difference of the maximum principal strain and the maximum shear strain, when comparing the frontal and back surface for the 20-mm experiments, was 11.1% and 6.6%, respectively.

The contours of the out-of-plane displacement, the maximum principal Lagrangian strain, and the shear Lagrangian strain at particular times when the PDMS sample's back surface was exposed to the shock wave, are shown in Figure 13. The out-of-plane displacement was lower on the back surface than the front surface. The peak maximum principal Lagrangian strain was in the range of 0.05 – 0.12 at the selected locations on the front surface, while the range for the back surface was 0.04 – 0.11. The peak shear strain range was 0 – 0.046 at the selected locations for front surface, and the range was 0 – 0.043 at the selected locations for the back surface.

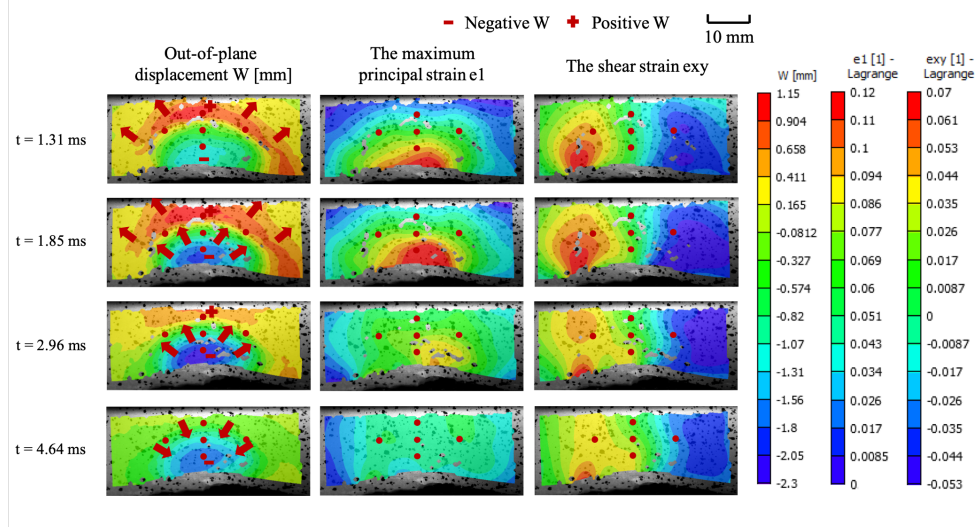


Figure 12: The contours of out-of-plane displacement (W), the maximum principal Lagrangian strain ($e1$), and the shear Lagrangian strain (exy) on the airfoil-shaped PDMS sample's **frontal** surface. Various time points ranging from 1.31 ms – 4.64 ms are shown. Negative W is compression, and positive W is protrusion. The arrows show the changing trend of the positive or negative area. The red dots show the locations for F1 – F5.

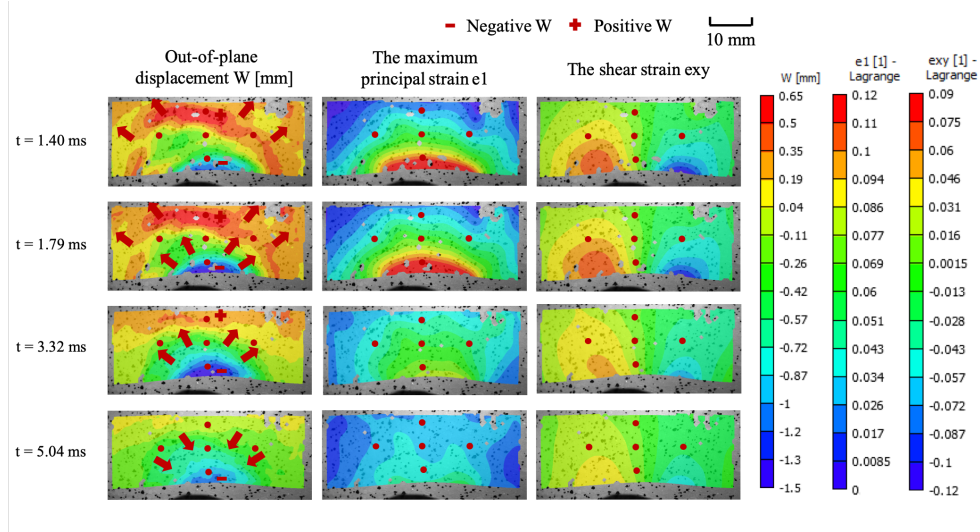


Figure 13: The contours of out-of-plane displacement (W), the maximum principal Lagrangian strain ($e1$), and the shear Lagrangian strain (exy) on the airfoil-shaped PDMS sample's **back** surface. Various time points ranging from 1.40 ms – 5.04 ms are shown. Negative W is compression, and positive W is protrusion. The arrows show the changing trend of the positive or negative area. The red dots show the locations for B1 – B5.

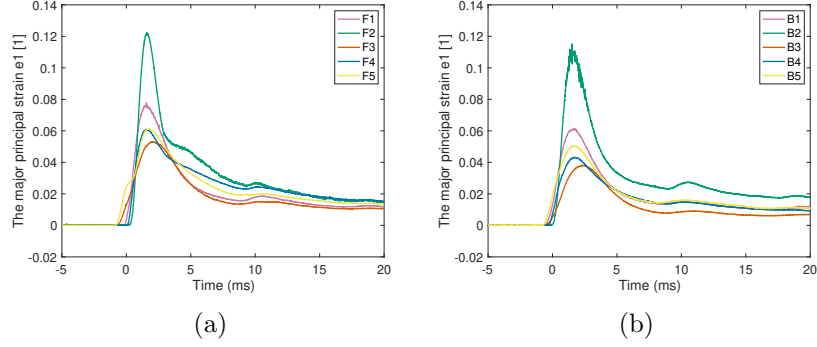


Figure 14: The averaged maximum principal Lagrangian strain at selected locations on the (a) **frontal** surface and (b) **back** surface.

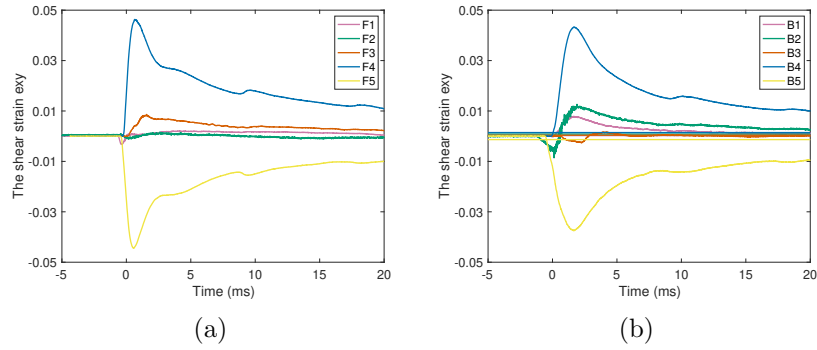


Figure 15: The averaged shear Lagrangian strain at selected locations on the (a) **frontal** surface and (b) **back** surface.

The averaged maximum principal strain at location F1 – F5 and B1 – B5 are shown in Figure 14 and the shear strain results are shown in Figure 15. The highest maximum principal strain is located at F2 and B2, and the highest shear strain locate at F4, F5, B4, and B5. Both averaged maximum principal strain and shear strain are higher on the frontal surface than the back surface.

3.3. Frequency of Oscillation

A comparison of the out-of-plane displacement results showed high frequency oscillations in all experiments that occurred after 8 ms, following the first peak out-of-plane displacement. The oscillations are more distinct when the back surface was exposed to the shock wave, which implied that the

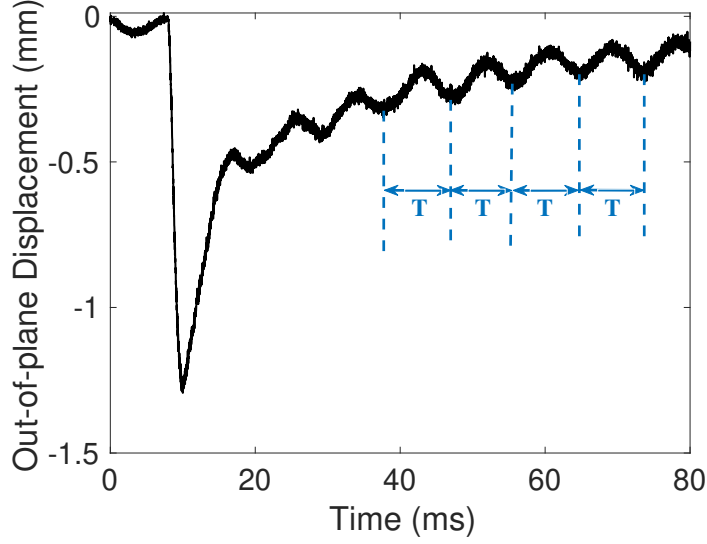


Figure 16: Period of oscillation (T) superimposed on the out-of-plane displacement, at back surface location F2.

sample's geometric differences influenced the deformation. To analyze the frequency of oscillation, the period of oscillation was first calculated from all out-of-plane displacement curves. Figure 16 illustrates how the period of oscillation was measured, using one result from the back surface experiment at a distance of 20-mm. The period of oscillation was measured for all experiments and at locations F1 – F5 and B1 – B5. Table 2 summarizes the averaged period of oscillation, along with the associated standard deviation. The averaged period of oscillation were consistent, across all combinations of the surface tested. Additionally, small standard deviations were obtained. The averaged frequency of oscillation across all experiments was 113.9 ± 2.7 Hz.

3.4. Finite Element Modeling Results

The predicted pressures in zones B, C, and D, shown in Figure 17, were applied in the positive z-axis direction during the transient structural analysis. Negative pressure of -63 kPa, was found on zone D. The FE simulation ran for 16 ms. Although not shown in Figure 17, a pressure of 0 kPa was utilized from 4 ms to 16 ms.

Out-of-plane displacement can be predicted by the transient structural

Table 2: Period and frequency details for the airfoil-shaped PDMS sample.

Surface	Number of Measured Periods	Averaged Period of Oscillation (s)	Standard Deviation for the Period of Oscillation (s)	Frequency (Hz)
Frontal	20	0.00872	0.00028	114.7
Back	20	0.00885	0.000148	113.0

analysis. A comparison of W at locations F1 – F5, from the 3D-DIC experiment and FE simulation is shown in Figure 18. Both negative (compression) and positive (protrusion) were captured by the FE simulation. The negative displacement at locations F1 and F2, from simulation, matched well with the experimental results. At location F3 – F5, the positive displacement provided by the simulation does not match well with the experiment after 2 ms (i.e. when the out-of-plane displacement starts to decrease). One possible reason is that the pressure applied on the surface was simplified, for the FE simulation.

A new finding from the FE simulation is that the protrusion on the sample surface, caused by the shock wave propagating through the sample, is due to a semicircular area of negative pressure generated on the surface. The negative pressure and positive out-of-plane displacement showed up in the same semicircular area. The out-of-plane displacement contours from both experiment and simulation are shown in Figure 19. The transient structural analysis provided a prediction of the out-of-plane displacement on the surface, which showed the same trend of compression in the center and protrusion in the semicircular area, when compared with the 3D-DIC experiments. A preliminary study showed that without the negative pressure applied on the surface, the FE simulation results will not yield any protrusion. Thus, the protrusion was not due to the compression in the center of the sample.

3.5. Dynamic Elastic Modulus

From this study, the dynamic elastic modulus for 1:70 PDMS is 19 kPa due to shock wave loading. This elastic modulus, for PDMS with a ratio of 1:70 subjected to high strain rates, has not been reported in literature.

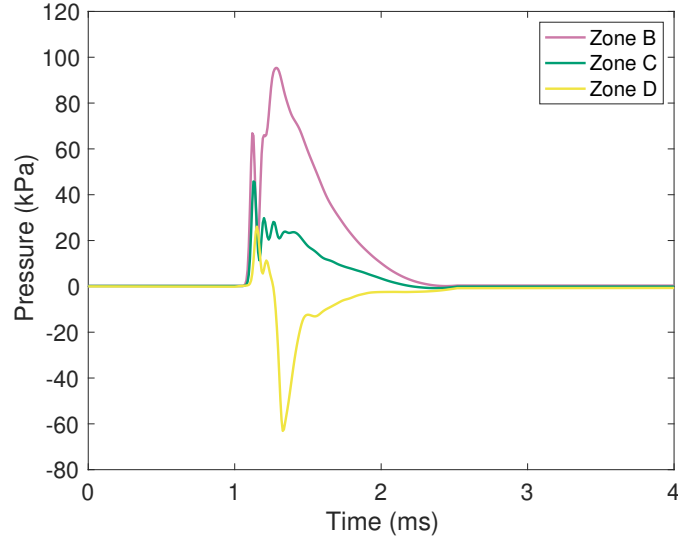


Figure 17: Pressure applied on the surface of the airfoil-shaped PDMS sample.

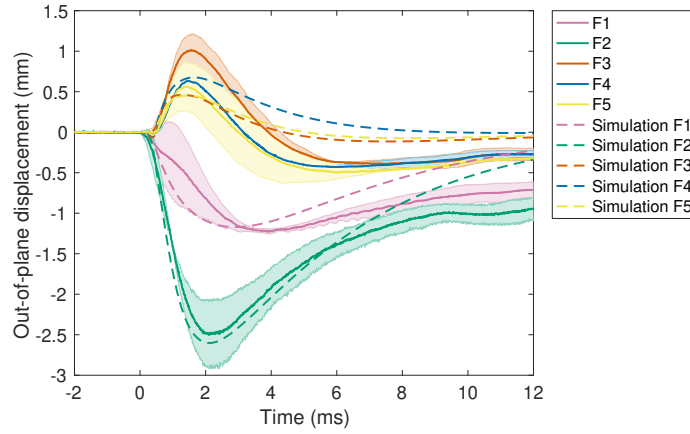


Figure 18: The averaged out-of-plane displacement at locations F1 – F5 (from 3D-DIC) compared with FE simulation, on the frontal surface. The dash lines show the out-of-plane displacement from the simulation, taken at the same location as the experiment.

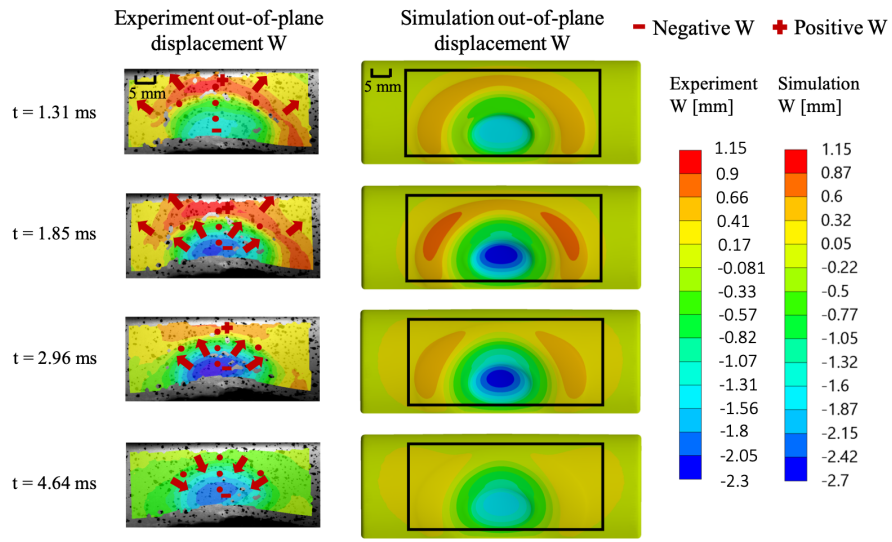


Figure 19: Comparison of out-of-plane displacement (W) contours between the 3D-DIC experiment and FE simulation, at different time steps. The bounding box outlined in black, for the simulation contours, correspond to the perimeter of the rectangular region containing the DIC contours.

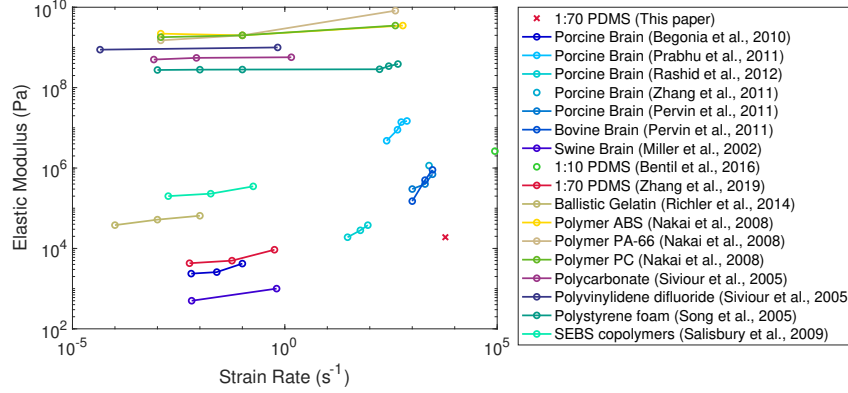


Figure 20: The comparison of elastic modulus from this study with brain tissue and other soft materials in the literature.

Figure 20 represents the superposition of elastic modulus versus strain rate from the literature, for soft materials and brain tissue. 1:70 PDMS shows an agreement of elastic modulus at low strain rates, when compared with the brain tissue in unconfined compression experiments (Zhang et al., 2019; McCarty et al., 2019). However, the elastic modulus for 1:70 PDMS exposed to a shock wave is lower than brain tissue. As a result, features of the time-history for the out-of-plane displacement (e.g. location of the peak and duration) may be different when compared with the brain, which may therefore influence brain injury predictions. Thus, the mismatch in the elastic modulus suggests that a ratio of 1:70 may not be ideal when using PDMS as a brain surrogate in high strain rate experiments.

4. Discussion and Conclusion

Utilization of improvised explosive devices has brought blast-induced traumatic brain injuries study into attention. The use of a surrogate brain in bTBI studies requires knowledge of the dynamic behavior, to ensure a biofidelic response due to shock wave exposure. However, the mechanical response of surrogate brains due to shock wave loading remains unknown (Hossain, 2010; Chanda et al., 2018; Alley et al., 2011; Mata et al., 2005; Zhang et al., 2007). Thus, in this paper, displacement and strain surface changes of a PDMS brain surrogate, when exposed to a shock wave, were experimentally and numerically investigated to extract the dynamic mechanical

properties. The dynamic properties are needed to calibrate FE models of the surrogate brain in bTBI simulations.

An airfoil shape was chosen for the brain surrogate, since this geometry mimics the shape of a pig brain. Although the mold created for the brain surrogate was handmade using an aluminum can, the airfoil coordinates were printed and carefully aligned so that the curved surface is the same as the modified NACA 2414 airfoil, which resembles the pig brain. To our knowledge, this is the first time that an airfoil-shaped brain surrogate has been utilized in the literature to understand deformation of a soft material due to shock wave exposure.

The experiments were performed using a compression-driven shock tube that was coupled with high-speed cameras to facilitate 3D-DIC analysis. The 3D-DIC analysis provided a non-contact technique for capturing the displacement and strain of the PDMS sample, under shock wave loading. Selected points on the PDMS sample's surface was used to plot the time-history of out-of-plane displacement. Coupling the results from 3D-DIC analysis with FE modeling facilitated calculation of the elastic modulus, for 1:70 PDMS ratio at high strain rates on the order of $6 \times 10^3 \text{ s}^{-1}$. The magnitude of the elastic modulus for 1:70 PDMS ratio was 98.3% lower than the tangent modulus of porcine brain subjected to uniaxial compression, in split Hopkinson pressure bar (SHPB) experiments by Zhang et al. (2011) at high strain rates on the order of $2.5 \times 10^3 \text{ s}^{-1}$. The tangent modulus calculated by Zhang et al. (2011) was 1149.6 kPa, for brain tissue at 37°C and strained to 20%. Just as the brain, 1:70 PDMS also had a similar increasing trend of elastic modulus with increased strain rate. In determining the suitability of PDMS as a brain surrogate in blast studies, the results from this study suggests that a lower ratio for PDMS is needed to reduce the mismatch in the elastic modulus when compared with the brain and yield a comparable deformation (e.g. out-of-plane displacement). Future research will examine the optimal ratio for PDMS used as a brain surrogate for blast impact studies.

Negative pressure was found in the simulation of flow field, when analyzing the surface of the PDMS due to shock wave exposure. Thus, further investigation into the negative pressure and its influence on causing soft materials to protrude will add knowledge for understanding bTBI. The extent of protrusion, if PDMS is to be used as a surrogate brain inside a surrogate skull, remains unknown and will be addressed in the future. However, Alley et al. (2011) found that the PDMS polymer provided a lower stiffness and highly viscous representation of brain tissue, when used in a confined

blast wave experiment. Thus, PDMS' deformations are expected to be higher when compared with the inhomogeneous brain tissue (Rashid et al., 2012b; Wen, 2003).

The contour plots for the maximum principal strain showed that the geometric differences between the frontal and back surface influenced the strain distribution. Distortion occurred on the PDMS surface, as captured by the contour plots for shear Lagrangian strain. As a result, an isochoric representation for the PDMS, was the physical motivation to understand the deformation due to shock wave exposure. An isochoric deformation implies that the volume of the PDMS material is preserved during shock wave exposure. Volume was preserved since the PDMS was not placed in an organic solvent to induce swelling. Thus, regions of compression and protrusion existed simultaneously on the PDMS surface to facilitate keeping the volume constant. At the microstructural level, the polymer chains coiled in the compressive region and tended to stretch in the protrusion region (Kausch and Plummer, 1994; Caruso et al., 2009). These complementary behaviors, for the polymer chains, may be attributed to PDMS being classified as an incompressible material with Poisson's ratio of 0.499 for strains below 45% (Müller et al., 2019; Johnston et al., 2014). Since the strains in this study did not exceed 14%, the airfoil shaped PDMS was incompressible and therefore subjected to isochoric deformation.

Polydimethylsiloxane (PDMS) is a temperature sensitive material, with an operational temperature range of -45°C to 200°C (-49°F to 392°F) (Corn-ing, 2020). However, the experiments were conducted at laboratory temperature (i.e. 21°C) to facilitate future research comparing the results with Zhang et al. (2019) and McCarty et al. (2019); who conducted experiments with brain surrogates and brain tissues at the same temperature but under quasistatic conditions. Our future work will also examine the response of brain tissue exposed to shock waves at a laboratory temperature of 21°C , to correlate the brain's dynamic mechanical response with the PDMS results presented in this study. Rashid et al. (2012d) found that there was not a statistically significant difference in the mechanical properties of brain tissue subjected to unconfined compression when tested at room temperature versus body temperature. This lack of statistical significant difference was true for experiments conducted at short durations (< 18 ms) and strain rates that exceeded 30/s. Since the shock wave experiments presented in this study is a form of unconfined compression and also consists of short durations (< 3 ms), with strain rates that exceed 30/s, room temperature was chosen for

convenience. Thus, future comparison of the mechanical properties for the brain surrogate and brain tissue, exposed to shock waves at room temperature, may be similar to comparing the mechanical properties of the brain surrogate with the *in vivo* brain at body temperature. To increase the applicability of the comparison, future shock wave exposure experiments will need to be conducted at room temperature using a brain surrogate and brain tissue that is encapsulated by a surrogate skull.

The suitability of PDMS as a surrogate material for the brain, in shock wave experiments and bTBI studies, will require multiscale research using *in vivo* brains. The macrostructural response of the brain surrogate and the *in vivo* brain would need to be related to changes in the brain's microstructural architecture. This work presents one of the first steps, which is to investigate the macrostructural response (i.e. deformation behavior) of a brain surrogate exposed to a shock wave, for future comparison with an actual brain. The next steps will require the development of a surrogate brain with the structural complexity (e.g. addition of vasculature, gray matter, white matter, ventricles, etc.) included, such that the heterogeneous and anisotropic features of the brain can be incorporated. As a result, the brain surrogate can exhibit deformation behavior mimicking the macrostructural response of an actual brain. Future steps would require correlating the deformation of the brain surrogate at the macroscale (i.e organ level) with the brain's severity of damage at the microscale (i.e. cellular level), to facilitate understanding of bTBI. The ultimate goal of developing this biofidelic brain surrogate is for use in a headform by researchers that are unable to conduct blast experiments with an actual brain tissue or an animal model. In this way, deformation of the brain surrogate within the headform can be used in bTBI experiments to predict the severity of injury or assess the effectiveness of personal protective equipment designed to mitigate blast-related injury.

Limitations of this study, which influenced the reported findings, were attributed to the restricted experimental setup and also the error from the measurements. For instance, the high-speed cameras were positioned 45° clockwise from horizontal. At this angle, the center area for the frontal PDMS surface would be obstructed by the end of the shock tube's driven section if the sample was placed at distance less than 20-mm away from the shock tube exit. Increasing the angle of the cameras was not feasible since it would increase the stress on the cameras' supports. Thus, the 20-mm distance was applied because this was the minimal distance that would eliminate the obstruction of the PDMS surface by the end of the shock tube's

driven section. Since the shock wave’s pressure-time waveform changes as the wave moves away from the shock tube exit (Kuriakose et al., 2016), the results presented in this study are for the case of a wave that interacts with the PDMS placed at a distance of 20-mm. The pressure-time trace measured by the pressure transducers showed that the shock wave created by the shock tube was repeatable, as evidenced by the small standard deviation in Figure 9.

The projection error, which measures correlation accuracy during 3D-DIC analysis, will influence the measurement errors for the out-of-plane displacements. Using the default values in VIC-3D, for the subset and step size, yielded the lowest projection error. The averaged projection error was 0.126 ± 0.0044 for front surface and 0.142 ± 0.01 for the back surface. The error values are attributed to a combination of the depth of field settings and the curvature of the airfoil sample’s surface. Specifically, large deformations would yield images that were slightly blurred since these images were outside the depth of field. Thus, increasing the projection error since the speckles from the blurred images could not be correlated.

PDMS has been reported in the literature as a brain surrogate by Zhang et al. (2019); Alley et al. (2011); Hossain (2010). Thus, the use of PDMS as a brain surrogate is an improvement over other surrogate brains exposed to a shock wave in the literature such as water (Hua et al., 2014) and mineral oil (Selvan et al., 2013). However, the brain is a complex multiphasic structure composed of white matter (anisotropic) and gray matter (isotropic), blood vessels, membranes, voids, and fissures, all filled with or surrounded by cerebrospinal fluid. As such, the mechanical response varies between these tissue types, brain-region where specimen are extracted for experiments, and also the age and gender of the test subjects. Furthermore, the complex brain exhibits rate sensitivity, especially in the shock regime along with different sensitivities for a given deformation mode (e.g. compression, tension and shear) (Jin et al., 2013). As a result, limitations of using PDMS in this study are attributed to (i) shock tube experiments that did not consider multiaxial loading of PDMS and (ii) application of a simplistic linear elastic model for PDMS, to represent the complex multiaxial response of the anisotropic and viscoelastic brain. Given the aforementioned limitations, PDMS will need to be tuned in the future such that the response due to high rate multiaxial loading using shock waves will mimic that of the brain when subjected to various deformation modes (e.g. compression, tension, and shear). Additionally, the optimal constitutive model such as viscoelastic (Bentil and Dupaix, 2018,

2014; Zhang et al., 2019; Kohandel et al., 2005; Holzapfel and Simo, 1996; Zhang et al., 2016; Budday et al., 2017; Miller and Chinzei, 1997; Miller, 1999; Lin et al., 2009), hyperelastic (Upadhyay et al., 2020b; Voyiadjis and Samadi-Dooki, 2018; Rashid et al., 2012a; Shergold et al., 2006), and visco-hyperelastic (Upadhyay et al., 2020a; Matin et al., 2020; P Mohammed, 2014; Rashid et al., 2012a; Chafi et al., 2010), for describing the multiaxial and rate dependent behavior of PDMS and brain tissue when exposed to a shock wave, will need to be determined prior to finalizing a standardized brain surrogate for future blast-impact studies. Constitutive models accounting for different responses of brain in compression, tension and shear, as well as rate dependence/sensitivities, have recently emerged in the literature (Upadhyay et al., 2020b,a) and will also be considered in the future.

Despite the aforementioned limitations, some critical findings regarding the deformation behavior of an airfoil-shaped brain surrogate under shock wave loading could be made and are:

1. Both negative (compression) and positive (protrusion) out-of-plane displacement was found on the PDMS surface, regardless of orientation. The percentage difference between the magnitude of negative out-of-plane displacement and the positive out-of-plane displacement were 84.6% and 90.1% for the frontal surface and back surface, respectively.
2. The frequency of oscillation, for 1:70 ratio PDMS (Sylgard 184) disturbed by a shock wave, was 113.9 ± 2.7 Hz. The frequency of oscillation does not depend on the sample's geometry.
3. The positive out-of-plane displacement (protrusion), found from 3D-DIC analysis, is due to the negative pressure in a semicircular ring area. From the ANSYS Fluent simulations of the fluid field around the PDMS sample, a negative pressure with a peak of -63 kPa was found. By applying the transient structural FE analysis, without this negative pressure, no positive out-of-plane displacement occurred.
4. By utilizing 3D-DIC experimental and FE methods, the elastic modulus for 1:70 PDMS is 19 kPa under shock wave loading for a strain rate of 6020/s. The calculated elastic modulus of 19 kPa was 197.5% different than the dynamic elastic modulus of 3 MPa for 1:10 PDMS (Bentil et al., 2016).

The first three critical findings describe the factors (i.e. out-of-plane displacement peak and duration, frequency of oscillation, and negative pressure) that are important in understanding the mechanical response of soft materials exposed to shock wave loadings. The aforementioned factors may be used to explain the mechanism of damage to the soft material or injury to the tissue.

Acknowledgements

This research was financially supported by the Roy J. Carver Charitable Trust under Grant #18-5021 and is acknowledged gratefully. The research is also financially supported by Iowa State University through start-up funds to SA. Bentil, for which the authors are grateful.

Supplemental Materials

For optimal results during the 3D-DIC analysis using VIC-3D, the correlation criterion and setting for the gray value interpolation was normalized squared difference and 8-tap spline, respectively. A supplemental video, looping through the out-of-plane displacement W events, is also provided. Negative W implies compression of the airfoil-shaped PDMS sample's surface.

References

- Alley, M. D., Schimizzze, B. R., Son, S. F., January 2011. Experimental modeling of explosive blast-related traumatic brain injuries. *Neuroimage* 54 Suppl 1, S45–54.
- Ansys 17.0, 2019. Academic research mechanical release 17.0.
- Begonia, M. T., Prabhu, R., Liao, J., Horstemeyer, M. F., Williams, L. N., October 2010. The influence of strain rate dependency on the structure-property relations of porcine brain. *Annals of Biomedical Engineering* 38 (10), 3043–3057.
- Bentil, S., Ramesh, K., Nguyen, T., 2016. A Dynamic Inflation Test for Soft Materials. *Experimental Mechanics* 56 (5), 759.

Bentil, S. A., Dupaix, R. B., 2014. Exploring the mechanical behavior of degrading swine neural tissue at low strain rates via the fractional zener constitutive model. *Journal of the Mechanical Behavior of Biomedical Materials* 30, 83–90.

Bentil, S. A., Dupaix, R. B., 2018. Simulations of hydrogel-coated neural microelectrodes to assess biocompatibility improvement using strain as a metric for micromotion. *Biomedical Physics & Engineering Express* 4 (3), 035036.

URL <http://stacks.iop.org/2057-1976/4/i=3/a=035036>

Budday, S., Sommer, G., Holzapfel, G., Steinmann, P., Kuhl, E., July 2017. Viscoelastic parameter identification of human brain tissue. *Journal of the Mechanical Behavior of Biomedical Materials* 74.

Cao, R., Zhang, C., Mitkin, V. V., Lankford, M. F., Li, J., Zuo, Z., Meyer, C. H., Goyne, C. P., Ahlers, S. T., Stone, J. R., Hu, S., January 2019. Comprehensive characterization of cerebrovascular dysfunction in blast traumatic brain injury using photoacoustic microscopy. *Journal of Neurotrauma*.

Caruso, M. M., Davis, D. A., Shen, Q., Odom, S. A., Sottos, N. R., White, S. R., Moore, J. S., November 2009. Mechanically-induced chemical changes in polymeric materials. *Chemical Reviews* 109 (11), 5755–5798, publisher: American Chemical Society.

URL <https://doi.org/10.1021/cr9001353>

Cernak, I., Noble-Haeusslein, L., 2010. Traumatic brain injury: an overview of pathobiology with emphasis on military populations. *Journal of Cerebral Blood Flow & Metabolism* 30 (2), 255.

URL <http://search.ebscohost.com/login.aspx?direct=true&db=a9h&AN=47846416&site=>

Chafi, M. S., Karami, G., Ziejewski, M., February 2010. Biomechanical assessment of brain dynamic responses due to blast pressure waves. *Annals of Biomedical Engineering* 38 (2), 490–504.

Chanda, A., Callaway, C., Clifton, C., Unnikrishnan, V., December 2018. Biofidelic human brain tissue surrogates. *Mechanics of Advanced Materials and Structures* 25 (15), 1335–1341.

URL <https://doi.org/10.1080/15376494.2016.1143749>

- Chandra, N., Ganpule, S., Kleinschmit, N. N., Feng, R., Holmberg, A. D., Sundaramurthy, A., Selvan, V., Alai, A., September 2012. Evolution of blast wave profiles in simulated air blasts: experiment and computational modeling. *Shock Waves* 22, 403–415.
URL <https://doi.org/10.1007/s00193-012-0399-2>
- Chandra, N., Sundaramurthy, A., Gupta, R. K., 2017. Validation of laboratory animal and surrogate human models in primary blast injury studies. *Military Medicine* 182, 105–113.
- Cho, H. J., Sajja, V. S. S. S., VandeVord, P. J., Lee, Y. W., December 2013. Blast induces oxidative stress, inflammation, neuronal loss and subsequent short-term memory impairment in rats. *Neuroscience* 253, 9–20.
URL <http://www.sciencedirect.com/science/article/pii/S0306452213007252>
- Clemedson, C.-J., April 1956. Shock wave transmission to the central nervous system. *Acta Physiologica Scandinavica* 37 (2), 204–214.
- Clemedson, C. J., Hultman, H. I., June 1954. Air embolism and the cause of death in blast injury. *Mil Surg* 114 (6), 424–437.
- Corning, D., 2018. Sylgard 184 silicone elastomer data sheet.
URL <https://consumer.dow.com/content/dam/dcc/documents/en-us/productdatasheet/11/11-31/11-3184-sylgard-184-elastomer.pdf?iframe=true>
- Corning, D., 2020. Sylgard 184 silicone elastomer.
- Evans, S. L., Holt, C. A., July 2009. Measuring the mechanical properties of human skin in vivo using digital image correlation and finite element modelling. *The Journal of Strain Analysis for Engineering Design* 44 (5), 337–345.
URL <https://doi.org/10.1243/03093247JSA488>
- Ganpule, S., Alai, A., Plougouven, E., Chandra, N., June 2013. Mechanics of blast loading on the head models in the study of traumatic brain injury using experimental and computational approaches. *Biomechanics and Modeling in Mechanobiology* 12 (3), 511–531.
- Ghajari, M., Hellyer, P. J., Sharp, D. J., Feb. 2017. Computational modelling of traumatic brain injury predicts the location of chronic traumatic

- encephalopathy pathology. *Brain* 140 (2), 333–343.
URL <https://academic.oup.com/brain/article/140/2/333/2770746/Computational-model>
- Grassi, L., Väänänen, S. P., Yavari, S. A., Jurvelin, J. S., Weinans, H., Ristinmaa, M., Zadpoor, A. A., Isaksson, H., November 2014. Full-field strain measurement during mechanical testing of the human femur at physiologically relevant strain rates. *Journal of Biomechanical Engineering* 136 (11).
- Gurev, V., Pathmanathan, P., Fattebert, J.-L., Wen, H.-F., Magerlein, J., Gray, R. A., Richards, D. F., Rice, J. J., August 2015. A high-resolution computational model of the deforming human heart. *Biomechanics and Modeling in Mechanobiology* 14 (4), 829–849.
- Hokka, M., Mirow, N., Nagel, H., Iqrsusi, M., Vogt, S., Kuokkala, V.-T., July 2015. In-vivo deformation measurements of the human heart by 3d digital image correlation. *Journal of Biomechanics* 48 (10), 2217–2220.
- Holzapfel, G. A., Simo, J. C., August 1996. A new viscoelastic constitutive model for continuous media at finite thermomechanical changes. *International Journal of Solids and Structures* 33 (20), 3019–3034.
- Hong, Y., Sarntinoranont, M., Subhash, G., Canchi, S., King, M. A., January 2016. Localized tissue surrogate deformation due to controlled single bubble cavitation. *Experimental Mechanics* 56 (1), 97–109.
URL <https://doi.org/10.1007/s11340-015-0024-2>
- Hossain, S. G. M., August 2010. MATERIAL MODELING AND ANALYSIS FOR THE DEVELOPMENT OF a REALISTIC BLAST HEADFORM. Ph.D. thesis, University of Nebraska at Lincoln.
URL <http://digitalcommons.unl.edu/mechengdiss/12>
- Hua, Y., Kumar Akula, P., Gu, L., Berg, J., Nelson, C. A., February 2014. Experimental and numerical investigation of the mechanism of blast wave transmission through a surrogate head. *Journal of Computational and Nonlinear Dynamics* 9 (3), 031010–031010–9.
URL <http://dx.doi.org/10.1115/1.4026156>
- Iwaskiw, A. S., Ott, K. A., Armiger, R. S., Wickwire, A. C., Alphonse, V. D., Voo, L. M., Carneal, C. M., Merkle, A. C., Jan. 2018. The measurement

- of intracranial pressure and brain displacement due to short-duration dynamic overpressure loading. *Shock Waves* 28 (1), 63–83.
URL <https://doi.org/10.1007/s00193-017-0759-z>
- Jin, X., Zhu, F., Mao, H., Shen, M., Yang, K. H., November 2013. A comprehensive experimental study on material properties of human brain tissue. *Journal of Biomechanics* 46 (16), 2795–2801.
URL <https://www.sciencedirect.com/science/article/pii/S0021929013004107>
- Johnston, I. D., McCluskey, D. K., Tan, C. K. L., Tracey, M. C., March 2014. Mechanical characterization of bulk sylgard 184 for microfluidics and microengineering. *Journal of Micromechanics and Microengineering* 24, 035017.
URL <http://adsabs.harvard.edu/abs/2014JMiMi..24c5017J>
- Kamnaksh, A., Kovesdi, E., Kwon, S.-K., Wingo, D., Ahmed, F., Grunberg, N. E., Long, J., Agoston, D. V., October 2011. Factors affecting blast traumatic brain injury. *Journal of Neurotrauma* 28 (10), 2145–2153.
- Kausch, H. H., Plummer, C. J. G., September 1994. The role of individual chains in polymer deformation. *Polymer* 35 (18), 3848–3857.
URL <http://www.sciencedirect.com/science/article/pii/0032386194902674>
- Kohandel, M., Sivaloganathan, S., Tenti, G., Darvish, K., June 2005. Frequency dependence of complex moduli of brain tissue using a fractional zener model. *Physics in Medicine and Biology* 50 (12), 2799–2805.
- Kuriakose, M., Skotak, M., Misistia, A., Kahali, S., Sundaramurthy, A., Chandra, N., September 2016. Tailoring the blast exposure conditions in the shock tube for generating pure, primary shock waves: The end plate facilitates elimination of secondary loading of the specimen. *PLoS ONE* 11 (9).
URL <https://www.ncbi.nlm.nih.gov/pmc/articles/PMC5014318/>
- Lin, I., Ou, K., Liao, Y., Liu, Y., Chen, K., Zhang, X., October 2009. Viscoelastic characterization and modeling of polymer transducers for biological applications. *Journal of Microelectromechanical Systems* 18 (5), 1087–1099, conference Name: *Journal of Microelectromechanical Systems*.
- Lord, J. D., Penn, D., Whitehead, P., July 2008. The application of digital image correlation for measuring residual stress by incremental hole drilling.

- Applied Mechanics and Materials 13-14, 65–73.
URL <https://www.scientific.net/AMM.13-14.65>
- Mahoney, P., Carr, D., Arm, R., Gibb, I., Hunt, N., Delaney, R. J., March 2018. Ballistic impacts on an anatomically correct synthetic skull with a surrogate skin/soft tissue layer. *International Journal of Legal Medicine* 132 (2), 519–530.
URL <https://doi.org/10.1007/s00414-017-1737-9>
- Mata, A., Fleischman, A. J., Roy, S., December 2005. Characterization of polydimethylsiloxane (PDMS) properties for biomedical micro/nanosystems. *Biomedical Microdevices* 7 (4), 281–293.
URL <https://doi.org/10.1007/s10544-005-6070-2>
- Matin, Z., Moghimi Zand, M., Salmani Tehrani, M., Wendland, B. R., Dargazany, R., January 2020. A visco-hyperelastic constitutive model of short- and long-term viscous effects on isotropic soft tissues. *Proceedings of the Institution of Mechanical Engineers, Part C: Journal of Mechanical Engineering Science* 234 (1), 3–17, publisher: IMECHE.
URL <https://doi.org/10.1177/0954406219875771>
- McCarty, A. K., Zhang, L., Hansen, S., Jackson, W. J., Bentil, S. A., Dec. 2019. Viscoelastic properties of shock wave exposed brain tissue subjected to unconfined compression experiments. *Journal of the Mechanical Behavior of Biomedical Materials* 100, 103380.
- Mediavilla Varas, J., Philippens, M., Meijer, S. R., van den Berg, A. C., Sibma, P. C., van Bree, J. L. M. J., de Vries, D. V. W. M., September 2011. Physics of IED blast shock tube simulations for mTBI research. *Front Neurol* 2 (58).
URL <https://www.ncbi.nlm.nih.gov/pmc/articles/PMC3177142/>
- Miller, K., May 1999. Constitutive model of brain tissue suitable for finite element analysis of surgical procedures. *Journal of Biomechanics* 32 (5), 531–537.
URL <https://www.sciencedirect.com/science/article/pii/S002192909900010X>
- Miller, K., Chinzei, K., November 1997. Constitutive modelling of brain tissue: Experiment and theory. *Journal of Biomechanics* 30 (11), 1115–1121.
URL <https://www.sciencedirect.com/science/article/pii/S0021929097000924>

- Miller, K., Chinzei, K., April 2002. Mechanical properties of brain tissue in tension. *Journal of Biomechanics* 35 (4), 483–490.
- Müller, A., Wapler, M. C., Wallrabe, U., January 2019. A quick and accurate method to determine the poisson’s ratio and the coefficient of thermal expansion of PDMS. *Soft Matter* 15 (4), 779–784, publisher: The Royal Society of Chemistry.
URL <https://pubs.rsc.org/en/content/articlelanding/2019/sm/c8sm02105h>
- Nakai, K., Yokoyama, T., January 2008. Strain rate dependence of compressive stress-strain loops of several polymers. *Journal of Solid Mechanics and Materials Engineering* 2 (4), 557–566.
- Ottenio, M., Tran, D., Ní Annaidh, A., Gilchrist, M. D., Bruyère, K., January 2015. Strain rate and anisotropy effects on the tensile failure characteristics of human skin. *Journal of the Mechanical Behavior of Biomedical Materials* 41, 241–250.
- P Mohammed, M. A., March 2014. Visco-hyperelastic model for soft rubber-like materials. *Sains Malaysiana* 43, 451–457.
- Palanca, M., Tozzi, G., Cristofolini, L., January 2016. The use of digital image correlation in the biomechanical area: a review. *International Biomechanics* 3 (1), 1–21.
URL <https://doi.org/10.1080/23335432.2015.1117395>
- Payne, T., Mitchell, S., Bibb, R., Waters, M., January 2014. Initial validation of a relaxed human soft tissue simulant for sports impact surrogates. *Procedia Engineering* 72, 533–538.
URL <http://www.sciencedirect.com/science/article/pii/S1877705814006080>
- Payne, T., Mitchell, S., Bibb, R., Waters, M., January 2015. The evaluation of new multi-material human soft tissue simulants for sports impact surrogates. *Journal of the Mechanical Behavior of Biomedical Materials* 41, 336–356.
URL <http://www.sciencedirect.com/science/article/pii/S1751616114003026>
- Pervin, F., Chen, W. W., January 2011. Effect of inter-species, gender, and breeding on the mechanical behavior of brain tissue. *NeuroImage* 54 Suppl 1, S98–102.

Prabhu, R., Horstemeyer, M. F., Tucker, M. T., Marin, E. B., Bouvard, J. L., Sherburn, J. A., Liao, J., Williams, L. N., October 2011. Coupled experiment/finite element analysis on the mechanical response of porcine brain under high strain rates. *Journal of the Mechanical Behavior of Biomedical Materials* 4 (7), 1067–1080.

Rashid, B., Destrade, M., Gilchrist, M. D., November 2012a. Hyperelastic and viscoelastic properties of brain tissue in tension. *American Society of Mechanical Engineers* 2, 921–929.

URL <https://asmedigitalcollection.asme.org/IMECE/proceedings/IMECE2012/45189/92>

Rashid, B., Destrade, M., Gilchrist, M. D., November 2012b. Inhomogeneous deformation of brain tissue during tension tests. *Computational Materials Science* 64, 295–300.

URL <http://www.sciencedirect.com/science/article/pii/S0927025612003011>

Rashid, B., Destrade, M., Gilchrist, M. D., June 2012c. Mechanical characterization of brain tissue in compression at dynamic strain rates. *Journal of the Mechanical Behavior of Biomedical Materials* 10, 23–38.

Rashid, B., Destrade, M., Gilchrist, M. D., Oct. 2012d. Temperature effects on brain tissue in compression. *Journal of the Mechanical Behavior of Biomedical Materials* 14, 113–118.

Readnower, R. D., Chavko, M., Adeeb, S., Conroy, M. D., Pauly, J. R., McCarron, R. M., Sullivan, P. G., December 2010. Increase in blood-brain barrier permeability, oxidative stress, and activated microglia in a rat model of blast-induced traumatic brain injury. *Journal of Neuroscience Research* 88 (16), 3530–3539.

Richler, D., Rittel, D., June 2014. On the testing of the dynamic mechanical properties of soft gelatins. *Experimental Mechanics* 54 (5), 805–815.

Risling, M., Plantman, S., Angeria, M., Rostami, E., Bellander, B. M., Kirkegaard, M., Arborelius, U., Davidsson, J., January 2011. Mechanisms of blast induced brain injuries, experimental studies in rats. *NeuroImage* 54, S89–S97.

URL <http://www.sciencedirect.com/science/article/pii/S1053811910007639>

- Salisbury, C. P., Cronin, D. S., January 2009. Mechanical properties of ballistic gelatin at high deformation rates. *Experimental Mechanics* 49 (6), 829.
- Säljö, A., Arrhén, F., Bolouri, H., Mayorga, M., Hamberger, A., December 2008. Neuropathology and pressure in the pig brain resulting from low-impulse noise exposure. *Journal of Neurotrauma* 25 (12), 1397–1406.
- Sarntinoranont, M., Lee, S. J., Hong, Y., King, M. A., Subhash, G., Kwon, J., Moore, D. F., October 2011. High-strain-rate brain injury model using submerged acute rat brain tissue slices. *Journal of Neurotrauma* 29 (2), 418–429, publisher: Mary Ann Liebert, Inc., publishers.
URL <https://www.liebertpub.com/doi/full/10.1089/neu.2011.1772>
- Selvan, V., Ganpule, S., Kleinschmit, N., Chandra, N., June 2013. Blast wave loading pathways in heterogeneous material systems-experimental and numerical approaches. *Journal of Biomechanical Engineering* 135 (6), 61002–61014.
- Shergold, O. A., Fleck, N. A., Radford, D., September 2006. The uniaxial stress versus strain response of pig skin and silicone rubber at low and high strain rates. *International Journal of Impact Engineering* 32 (9), 1384–1402.
URL <https://www.sciencedirect.com/science/article/pii/S0734743X04002325>
- Shridharani, J. K., Wood, G. W., Panzer, M. B., Capehart, B. P., Nyein, M. K., Radovitzky, R. A., Bass, C. R. d., 2012. Porcine head response to blast. *Frontiers in Neurology* 3, 70.
- Siviour, C. R., Walley, S. M., Proud, W. G., Field, J. E., December 2005. The high strain rate compressive behaviour of polycarbonate and polyvinylidene difluoride. *Polymer* 46 (26), 12546–12555.
- Song, B., Chen, W. W., Dou, S., Winfree, N. A., Kang, J. H., May 2005. Strain-rate effects on elastic and early cell-collapse responses of a polystyrene foam. *International Journal of Impact Engineering* 31 (5), 509–521.
- Stern, R. A., Riley, D. O., Daneshvar, D. H., Nowinski, C. J., Cantu, R. C., McKee, A. C., October 2011. Long-term consequences of repetitive brain

- trauma: Chronic traumatic encephalopathy. *PM R.* 3 (10), S460–S467.
URL <http://onlinelibrary.wiley.com/doi/abs/10.1016/j.pmrj.2011.08.008>
- Tan, X. G., Przekwas, A. J., Gupta, R. K., November 2016. Macro-micro biomechanics finite element modeling of brain injury under concussive loadings. ASME 2016 International Mechanical Engineering Congress and Exposition 3, V003T04A036.
URL <http://dx.doi.org/10.1115/IMECE2016-66218>
- Taylor, P. A., Ford, C. C., June 2009. Simulation of blast-induced early-time intracranial wave physics leading to traumatic brain injury. *Journal of Biomechanical Engineering* 131 (6), 061007.
- Taylor, P. A., Ludwigsen, J. S., Ford, C. C., March 2014. Investigation of blast-induced traumatic brain injury. *Brain Injury* 28 (7), 879–895.
- Tung, S.-H., Shih, M.-H., Kuo, J.-C., May 2010. Application of digital image correlation for anisotropic plastic deformation during tension testing. *Optics and Lasers in Engineering* 48 (5), 636–641.
URL <http://www.sciencedirect.com/science/article/pii/S0143816609002358>
- Upadhyay, K., Subhash, G., Spearot, D., September 2020a. Hyperelastic constitutive modeling of hydrogels based on primary deformation modes and validation under 3d stress states. *International Journal of Engineering Science* 154, 103314.
URL <https://www.sciencedirect.com/science/article/pii/S0020722520301026>
- Upadhyay, K., Subhash, G., Spearot, D., February 2020b. Visco-hyperelastic constitutive modeling of strain rate sensitive soft materials. *Journal of the Mechanics and Physics of Solids* 135, 103777.
URL <https://www.sciencedirect.com/science/article/pii/S0022509619305307>
- VIC3D, 2017. Vic-3D (Version 8) Reference Manual. Correlated Solution, www.correlatedsolutions.com.
- Voyiadjis, G. Z., Samadi-Dooki, A., July 2018. Hyperelastic modeling of the human brain tissue: Effects of no-slip boundary condition and compressibility on the uniaxial deformation. *Journal of the Mechanical Behavior of Biomedical Materials* 83, 63–78.

- Wang, Y., Cuitiño, A. M., June 2002. Full-field measurements of heterogeneous deformation patterns on polymeric foams using digital image correlation. *International Journal of Solids and Structures* 39 (13), 3777–3796.
URL <http://www.sciencedirect.com/science/article/pii/S0020768302001762>
- Wang, Y., Ye, Z., Hu, X., Huang, J., Luo, Z., July 2010. Morphological changes of the neural cells after blast injury of spinal cord and neuroprotective effects of sodium beta-aescinate in rabbits. *Injury* 41 (7), 707–716.
- Wen, P., September 2003. The impact of inhomogeneous tissue anisotropy on potential distribution within head model. *Australasian Physics & Engineering Sciences in Medicine* 26 (3), 115.
URL <https://doi.org/10.1007/BF03178780>
- Wilcox, D. C., November 1988. Reassessment of the scale-determining equation for advanced turbulence models. *AIAA Journal* 26 (11), 1299–1310.
- Zhang, D., Arola, D., Eggleton, C., October 2002. Measurement of poisson’s ratio of bovine aorta using digital image correlation. *Proceedings of the Second Joint 24th Annual Conference and the Annual Fall Meeting of the Biomedical Engineering Society* [Engineering in Medicine and Biology 2, 1276–1277 vol.2.
- Zhang, H., Hayashi, T., Tsuru, K., Deguchi, K., Nagahara, M., Hayakawa, S., Nagai, M., Kamiya, T., Osaka, A., Abe, K., February 2007. Vascular endothelial growth factor promotes brain tissue regeneration with a novel biomaterial polydimethylsiloxane–tetraethoxysilane. *Brain Research* 1132, 29–35.
URL <http://www.sciencedirect.com/science/article/pii/S0006899306028630>
- Zhang, J., Yoganandan, N., Pintar, F. A., Guan, Y., Shender, B., Paskoff, G., Laud, P., February 2011. Effects of tissue preservation temperature on high strain-rate material properties of brain. *Journal of Biomechanics* 44 (3), 391–396.
- Zhang, J. T., Zhang, M., Li, S. X., Pavier, M. J., Smith, D. J., June 2016. Residual stresses created during curing of a polymer matrix composite using a viscoelastic model. *Composites Science and Technology* 130, 20–27.
URL <https://www.sciencedirect.com/science/article/pii/S0266353816302135>

- Zhang, L., Jackson, W. J., Bental, S. A., July 2019. The mechanical behavior of brain surrogates manufactured from silicone elastomers. *Journal of the Mechanical Behavior of Biomedical Materials* 95, 180–190.
URL <http://www.sciencedirect.com/science/article/pii/S1751616118316734>
- Zhang, Y., Yang, Y., Tang, H., Sun, W., Xiong, X., Smerin, D., Liu, J., May 2014. Hyperbaric oxygen therapy ameliorates local brain metabolism, brain edema and inflammatory response in a blast-induced traumatic brain injury model in rabbits. *Neurochemical Research* 39 (5), 950–960.
- Zhu, F., Skelton, P. L., Chou, C. C., Mao, H., Yang, K. H., King, A., March 2013. Biomechanical responses of a pig head under blast loading: a computational simulation. *International journal for numerical methods in biomedical engineering* 29 (3), 392–407.